

## **A Motion Compensation Approach for Oral and Maxillofacial Cone-beam Imaging**

Tao Sun\*

*Paul C. Lauterbur Research Center for Biomedical Imaging, Shenzhen Institutes of Advanced Technology, Chinese Academy of Science, China*

Reinhilde Jacobs

*OMFS-IMPACT, Department of Imaging and Pathology, KU Leuven, Belgium*

Ruben Pauwels

*Aarhus Institute of Advanced Studies, Aarhus University, Denmark*

Elisabeth Tijssens

*OMFS-IMPACT, Department of Imaging and Pathology, KU Leuven, Belgium*

Roger Fulton

*Faculty of Medicine and Health and School of Physics, University of Sydney, Australia*

Department of Medical Physics, Westmead Hospital, Westmead, Australia

Johan Nuyts

*Medical Imaging Research Center and Department of Nuclear Medicine, KU Leuven, Belgium*

\*Corresponding author: tao.sun@siat.ac.cn

## **Abstract**

**Purpose:** Patient movement affects image quality in oral and maxillofacial cone-beam CT imaging. While many efforts are made to minimize the possibility of motion during a scan, relatively little attention has been given to motion compensation after the acquisition.

**Methods:** In a previous study, we proposed a retrospective motion compensation approach for helical head CT imaging, which iteratively estimates and compensates for rigid head motion. This study reports on an extension of the previous method to cone-beam CT imaging. To address the issue of the limited field-of-view, improvements were made to the original method. The proposed motion estimation/ motion compensation (ME/MC) method was evaluated with simulations, phantom and patient studies. Two experts in dentomaxillofacial radiology assessed the diagnostic importance of the achieved motion artifact suppression.

**Results:** The quality of the reconstructed images was improved after motion compensation, and most of the image artifacts were eliminated. Quantitative analysis by comparison to a reference image (simulation and phantom) and by calculation of a sharpness metric agreed with the qualitative observation.

**Conclusions:** The proposed method has the potential to be clinically applied.

**Keywords:** cone-beam Computed Tomography (CT), oral and maxillofacial imaging, motion estimation, motion compensation.

## 1. Introduction

Patient motion is one of the main causes of image artifacts in oral and maxillofacial imaging. Unlike clinical helical CT, dental imaging uses cone-beam CT (CBCT) most commonly, which typically requires longer scan time and thus has a higher probability of patient movement. It was shown that, due to fear of the tube/detector movement, some patients in particular children, move their head during a scan <sup>1</sup>. Also, it is difficult to prevent aged patients with brain disorders such as Parkinson's disease, from moving <sup>2</sup>. In a study, it was found that about 18% of the pediatric patients and 24% of aged subjects were likely to move sufficiently to induce motion artifacts in the reconstructed images <sup>3</sup>.

The motion artifacts in the reconstructed image can degrade the image quality, adversely affecting diagnosis or treatment planning <sup>4</sup>. Even when the motion is too small to be noticed directly, it may still cause a significant resolution loss in the reconstructed image. In such case, the resolution of the flat panel detector would not be the limiting factor of the image resolution, but the motion is. Further problems arise when metal implants are present together with motion <sup>5</sup>. To obtain an image without artifacts, sometimes a retake of the scan may be required, which inevitably causes additional radiation dose to the subject.

Many efforts have been made to prevent patient motion. It is often suggested an examiner should instruct the subjects to close their eyes and be prepared for the scanner movement prior to the acquisition <sup>6</sup>. Patients are sometimes immobilized using a head strap, and/or a chin holder. However, solely relying on the hardware to fix the head may not prevent all potential movements.

Relatively few works have been published on methods for reducing motion artifacts in the reconstructed image. One recent work demonstrated the potential to track the head movement with the help of an optical camera <sup>7</sup>. Another work aimed to estimate and compensate the motion retrospectively, by enforcing the local consistent contours of teeth <sup>8</sup>. On the other hand, there are

several existing retrospective correction methods focusing on head CT imaging<sup>9-13</sup>. Most of these works obtained the motion parameters either by maximizing the data-consistency between the object and projections or maximizing a metric such as sharpness of image. Then a compensation was performed with estimated motion.

Similar to above retrospective methods, we previously described an iterative method to estimate and compensate the head motion in helical CT imaging<sup>14</sup>. In this work, we extended that approach to oral and maxillofacial CBCT imaging. We made certain improvements to tackle the new challenges. The proposed method was evaluated using simulations as well as a phantom scan. Additionally, a patient scan with motion artifacts was used to further validate the proposed method for its clinical applicability by two experienced dentists trained in dentomaxillofacial radiology. Note that an initial effort was published as a conference proceeding, which presented simulation study only and a different implementation of methods<sup>15</sup>.

## **2. MATERIALS AND METHODS**

### **2.A Revisit of the previous approach**

Let us first define the coordinate systems of a virtual CBCT imaging system in Figure 1. One is the detector coordinate system, which is used when estimating the motion parameters. Another is the scanner coordinate system, which is used during motion compensation. Figure 2 gives a scheme of the motion estimation and compensation algorithm. An initial image is reconstructed from the measured projections without any motion correction. In our previous work, we assumed that the rigid pose of the measured object may be different for each projection view. Consequently, a rigid transformation representing the object pose was estimated for every view, by a 3D-2D registration process. Auxiliary projections are computed to enable an approximate analytical

calculation of the motion parameter at each iteration. Translation perpendicular to the detector was neglected because correcting for it was found to have negligible effect on reconstructed image quality. The other five rigid parameters were estimated in a sequential way at each given projection view (first translation, then rotation). The new estimated parameter values were used immediately when estimating the value of the next parameter. This motion estimate for all projection views completed the update of the rigid motion at one iteration, labeled as motion estimation (“ME” block in Figure2).

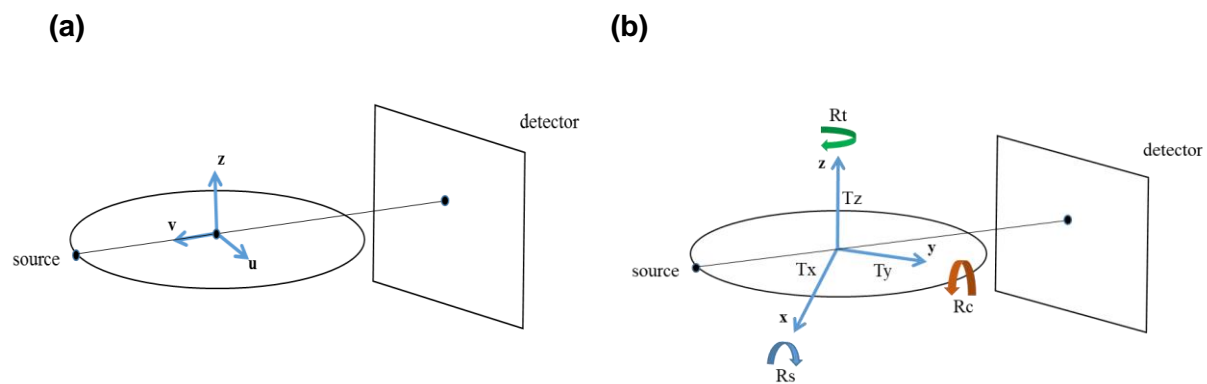


**Figure 1** For every view, the centers of (a) the detector and (b) scanner coordinate systems coincide with each other.  $T_x$ ,  $T_y$ ,  $T_z$  are translations along coordinate axes.  $R_t$ ,  $R_s$ ,  $R_c$  are rotations around coordinate axes.

A compensation for changes in pose during the scan was applied in the reconstruction by incorporating the motion into the system matrix (“MC” block in Figure 2). Ordered Subset Expectation Maximization<sup>16</sup> was used as the reconstruction algorithm. Instead of moving the reconstructing image in every view, rigid motion compensation was done by considering a coordinate system fixed to the object and incorporating the motion (now associated to the source-detector pair) into the system matrix. This corresponds to an arbitrary 3D motion of a virtual gantry around the object being scanned, created by the superposition of the inverse of the object motion on the X-ray source trajectory.

The motion estimate and motion-corrected image were alternately updated to increase the likelihood, and the iterations were stopped when the estimated motion seemed to have converged. A multiresolution approach was applied to accelerate the computation. For example, the starting resolution image level was  $4 \times 4 \times 4$ , i.e. down-sampling factor of four was applied in all directions. There was a resampling with a factor of two between adjacent levels. A similar multi-resolution approach can be also applied in the projection domain. The proposed approach has been shown to effectively suppress the motion artifacts in helical CT scans with different setups and various scanners <sup>14</sup>.

On completion of the iterative ME/MC process, a final reconstruction was performed using the final estimated motion. For this reconstruction, either a full iterative algorithm can be used with incorporating the motion. Alternatively, to speed up the calculation, an approximate circular FDK algorithm was implemented, where a first order motion compensation is obtained by taking the motion for each view into account in the back-projection step.

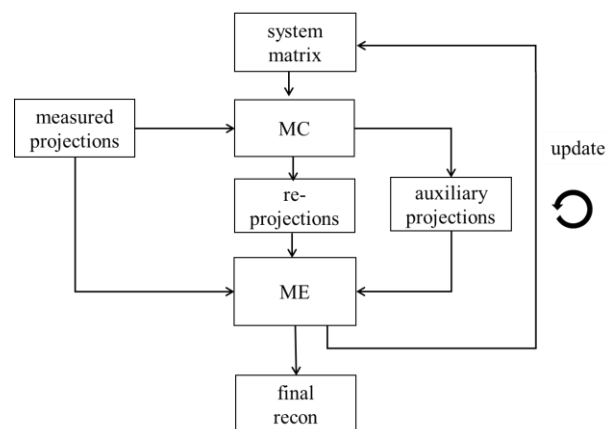


**Figure 2** Motion Estimation/ Motion Compensation (ME/MC) scheme in<sup>14</sup>. One iteration of ME/MC involves 1 ME step and 1 MC step. One ME step attempts to adjust the object pose at each view to minimize the difference between the measured projections and the re-projected object, with the help of auxiliary projections. One MC step compensates for the motion during the scan in the iterative reconstruction process, by incorporating the motion estimates into the system matrix.

## 2.B New challenges in oral and maxillofacial imaging

The main differences between CBCT and helical CT are the trajectory and the truncation. Dental CBCT uses a circular scanning orbit with constant axial field-of-view (FOV), whereas clinical CT uses a helical trajectory with strong axial truncation and a continuously changing axial FOV. For motion correction, a circular trajectory and constant axial field of view are expected to be less challenging than a helical one. On the other hand, dental CBCT is typically focused on small field of view and the acquired projections suffer from a strong transaxial truncation, whereas transaxial truncation is usually minor or absent in helical CT. This transaxial truncation is expected to adversely affect ME/MC. Specifically, the ME is based on re-projection, requiring a reconstructed image of the full object, which is not available in a region-of-interest (ROI) scan. In addition, the MC step uses an iterative reconstruction, which again requires a reconstructed full object during forward/back-projection. Hence, insufficient information outside the completely sampled ROI will induce errors. These errors introduce streak artifacts in the reconstructed image after every iteration, resulting in inaccurate estimated motion.

A related concern is that the information in the background, while not of clinical importance, is required by an iterative reconstruction algorithm. An analytical reconstruction algorithm such as Feldkamp-Davis-Kress (FDK <sup>17</sup>) can restrict the computations to the ROI, making it very efficient for such applications. In contrast, when an iterative reconstruction algorithm is used, the entire object must be reconstructed. Since our current motion compensation approach relies on iterative reconstruction, there is value in minimizing the amount of computations devoted to the background region, without compromising much on reducing the motion artifacts.

## 2.C Proposed improved ME/MC

To mitigate above issues, we propose two new improvements over the previous method below. The goal is reducing the effect of the transaxial truncation, by emphasizing the region-of-interest (containing teeth and bone) during the ME/MC, but not the background.

### 1. Feature-based motion estimation

Our previous method assumed no transaxial truncation in a scan. This is no longer valid for a ROI scan, as the object outside the ROI (background) does not contribute to all acquired views. The truncation artifacts typically result in blurring across the missing projection lines. By focusing on high frequency contents, we expect to reduce the influence of missing projection lines on the motion estimation. Therefore, we did not derive the motion based on the projections themselves but on the high-frequency parts of them.

To do so, we modified the original scheme by introducing a Laplacian of Gaussian operation on all projections (measured projections, re-projections, auxiliary projections). Hence only ME was modified accordingly, while the rest of the ME/MC process remained the same. For a given 2D projection view, we applied the Laplacian of Gaussian operator by applying the convolution kernel:

$$\text{LOG}(x, y) = -\frac{1}{\pi\sigma^4} \left[ 1 - \frac{x^2 + y^2}{2\sigma^2} \right] \exp\left( -\frac{x^2 + y^2}{2\sigma^2} \right)$$

where  $\sigma$  is Gaussian smoothing kernel width. A discrete kernel that approximates above function ( $\sigma=1.0$ , window size  $7 \times 7$ ) was used in the following study.

### 2. Patch-based reconstruction

First let us define the forward model of the acquisition. Assuming monochromatic radiation and ignoring scattering effect, the penalized Poisson log-likelihood function for the attenuation image  $\mu$  is:

$$L(\mu) = \sum_i y_i \ln \bar{y}_i(\mu) - \bar{y}_i(\mu) - \beta X(\mu) \quad \text{Eq. (1)}$$

where  $i$  is the index of the projection lines,  $y_i$  is the measured transmission scan at  $i$ ,  $\bar{y}_i(\mu)$  is the estimated transmission scan at  $i$  computed from the attenuation image  $\mu$ ,  $X(\mu)$  is the regularization term and  $\beta$  is the weighting factor.

By maximizing Eq. 1, one can find the optimal attenuation image iteratively. For example, ignoring the regularization term, the update function of Maximum-Likelihood-Transmission-Reconstruction (MLTR <sup>18</sup>) is:

$$\mu_j^{new} = \mu_j + \frac{\sum_i c_{ij} (\bar{y}_i - y_i)}{\sum_i c_{ij} (\sum_k c_{ik}) \bar{y}_i} \quad \text{Eq. (2)}$$

where  $\mu_j$  is the linear attenuation coefficient at voxel  $j$ ,  $c_{ij}$  is the intersection length of projection line  $i$  with voxel  $j$ . Note that we drop the argument of  $\bar{y}_i$  for clarity. Motion compensation can be done by adjusting the system matrix on-the-fly, as explained in the Introduction.

Patch-based reconstruction approaches have been proposed for various applications in CT imaging <sup>18-21</sup>. The idea is that a reconstruction volume can be divided into interesting patches and not-so-important patches. For each of these patches a different resolution model can be defined. This will allow us to focus the computations more on the regions of interest. We defined two patches for dental ROI imaging (Figure 3): high-res patch – the patch containing the fully sampled ROI where a smaller voxel size was used; low-res patch – the patch comprising the remainder of the object where a coarser resolution model (the voxel size was 4 times larger in all 3 dimensions) was used. The modified update equation of MLTR with the capability to account for patches is:

$$\mu_j^{new} = \mu_j + \frac{a_j \sum_i c_{ij} (\bar{y}_i - y_i)}{\sum_i c_{ij} (\sum_k c_{ik} a_k) \bar{y}_i} \quad \text{Eq. (3)}$$

where

$$\begin{cases} a_j = 1 & \text{if } j \in \text{patch} \\ a_j = 0 & \text{if } j \notin \text{patch} \end{cases}$$

The voxel weighting factor  $a_j$  also plays an important role in convergence of the attenuation values at each voxel. The patches were updated sequentially, each patch was considered as a group of pixels in a grouped coordinate algorithm. Sequentially updating groups of pixels is known to improve convergence, as the denominator of the update steps will be smaller when the area of the updated patch is smaller.

Specifically, both ME and MC need to be adjusted for patch-based implementation. For ME, the re-projection process involved the forward projections with different resolutions for different patches. For MC (iterative reconstruction), each update of the image can be divided into 2 steps (Figure 3) – a first update performed only in the high-res patch, and a sequential update performed in low-res patch only. MLTR performed alternate updates for two patches (where the high-res patch update is with total-variation regularization). The rest of the ME/MC remained unchanged.

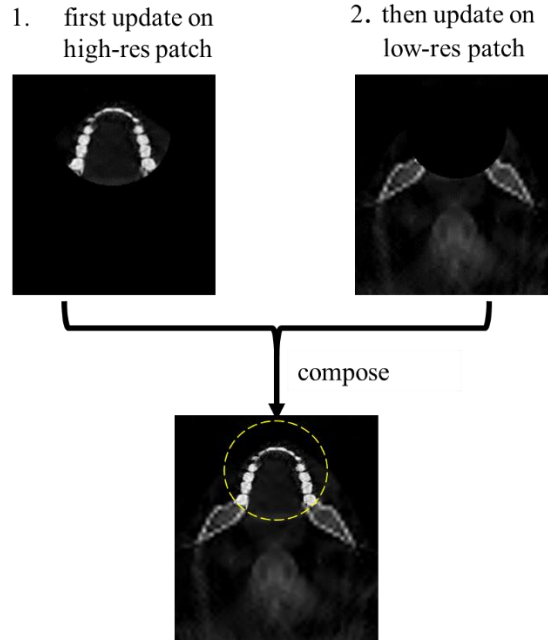


**Figure 3** Schematic representation of an iteration of the MC reconstruction. A first update was only performed in the high-res patch, and a sequential update was performed in the low-res patch. The dashed circle indicates the fully sampled FOV, i.e. high-res patch.

## 2.D Quantitative analysis

Besides visual comparison, we performed a quantitative comparison between the uncorrected, corrected and ground truth images. For the simulation and phantom studies, we computed the SSIM index<sup>22</sup> for both uncorrected and corrected images with respect to the truth image. Let us take the corrected image (MC) as example, SSIM index was calculated as:

$$\text{SSIM}(\text{REF}, \text{MC}) = \frac{(2\bar{\mu}_{\text{REF}}\bar{\mu}_{\text{MC}} + c_1)(2\sigma_{\text{REF-MC}} + c_2)}{(\bar{\mu}_{\text{REF}}^2 + \bar{\mu}_{\text{MC}}^2 + c_1)(\sigma_{\text{REF}}^2 + \sigma_{\text{MC}}^2 + c_2)}$$

where  $\bar{\mu}$  and  $\sigma$  represent the mean intensity and the variance of the image,  $\sigma_{\text{REF-MC}}$  is the covariance of two images. Term  $c_1=10^{-4} \text{ cm}^{-2}$  and  $c_2=3 \times 10^{-4} \text{ cm}^{-2}$  was set to stabilize the low intensities.

As for the patient study, since we did not have a ground truth image, we cannot calculate the SSIM index. We instead computed an image sharpness index, i.e. gradient variance, which was shown to be sensitive to motion artifacts<sup>13,23</sup>:

$$GV(\mu) = \sum_j \left( TV(\mu_j) - \frac{1}{N_v} \sum_j TV(\mu_j) \right)^2$$

$$TV(\mu_j) = \sqrt{\nabla_x(\mu_j)^2 + \nabla_y(\mu_j)^2 + \nabla_z(\mu_j)^2}$$

where  $N_v$  is total number of voxels,  $TV(\mu_j)$  is the l-2 norm of the image gradients. Motion would reduce the image sharpness and the corresponding gradient variance will be smaller for a motion-free image.

### 3. SIMULATIONS

#### 3.A Digitized phantom and motion

A digital phantom (Figure 4) was used in all simulations. It was discretized into an image of 256x256x70 voxels with a voxel size of 1x1x1 mm<sup>3</sup>. A detector with 200x80 detector pixels of 1x1 mm<sup>2</sup> was simulated to create the transaxially truncated projections. The distance between the X-ray source and the detector was 575 mm, the distance between the detector and the rotation center was 216.5 mm.

Two segments of head motion from a volunteer recorded over a 5 second period (in a CT scanner but without irradiation) were applied to the digital phantom to compute cone-beam projections. Of these two segments one was more abrupt and another more continuous, see Figure 5. The total number of views was 360 covering one full rotation. The projections were simulated with distance-driven projector<sup>24</sup>, which was also used later in the reconstruction. We assumed that the motion within one cone-beam projection view is negligible, hence there was no motion simulated within one projection view.

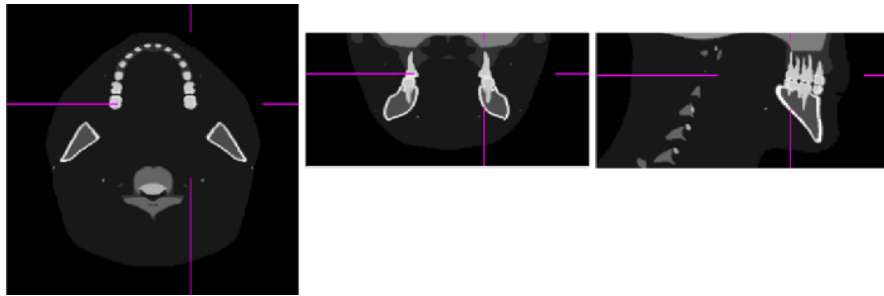


**Figure 4** The digital phantom that used in the simulations. For left to right: selected transaxial, coronal and sagittal view.

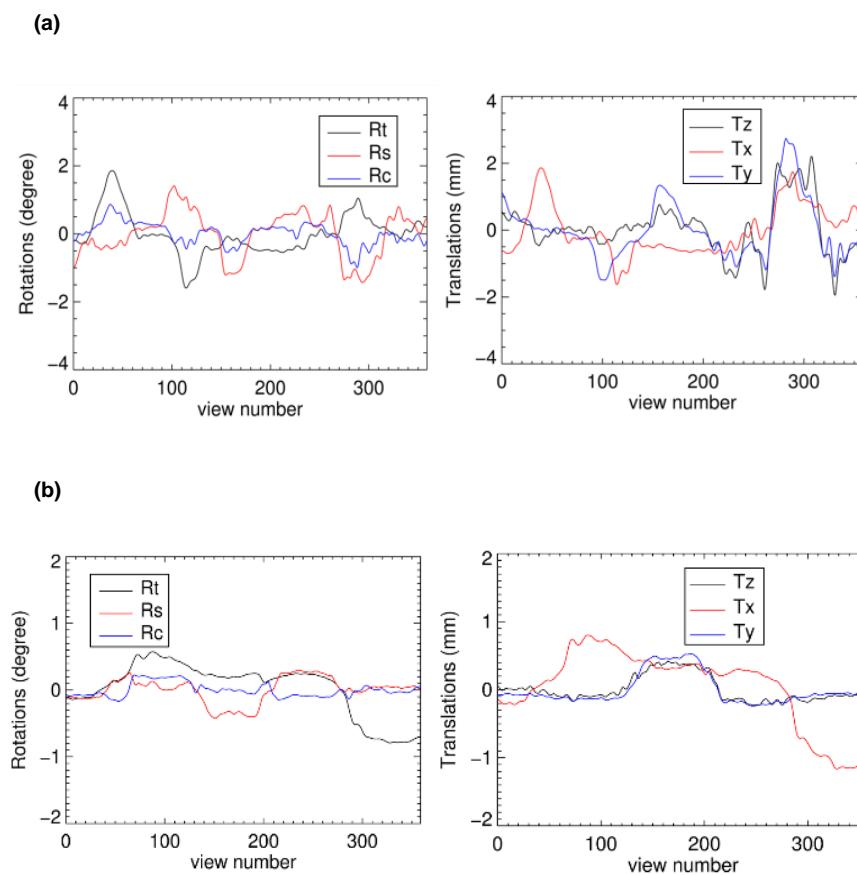


**Figure 5** The recorded motion segments used to generate the motion-contaminated projections. Motion (a) is more abrupt while (b) is more continuous.  $R_t$ ,  $R_s$ ,  $R_c$ ,  $T_z$ ,  $T_x$ ,  $T_y$  were defined in Figure 1. Details of how it was recorded can be found in <sup>25</sup>.

### 3.B Experiment design

We aimed to compare the image quality in three cases: one reconstructed with the compensation using the exact simulated motion as reference, one without any compensation, and one with the proposed compensation method. Details of how these images were obtained are listed below.

1. Reference image

The reference image was obtained with a cone-beam FDK algorithm with the exact simulated motion taken into account in the back-projection step. Note that ideally one should also adjust the filtering and pre-weighting in FDK algorithm. But since the motion amplitude is relatively small in most of the dental scans, we only applied a first-order compensation.

2. Image w/o compensation

A cone-beam FDK reconstruction was applied to the simulated motion-corrupted projections without any compensation.

3. Image with ME/MC

In one MC, high-res and low-res patches were updated in an interleaved fashion with 2 iterations and 40 subsets. The high-res patch had a resolution of  $1 \times 1 \times 1 \text{ mm}^3$ , while the low-res patch had  $4 \times 4 \times 4 \text{ mm}^3$ . In one ME, re-projection was done by combining the forward projections of the two patches (Section 2.C). The total number of iterations of ME/MC depends on each scan case. At each iteration, we computed the summed absolute difference between the measured projections and re-projections. When the reduction of the reprojection errors was less than a threshold (2% of the initial summed reprojection error), we stopped the iterations. A final corrected image was obtained with an FDK algorithm compensating for the estimated motion.

### 3.C Results

Figure 6 shows the resulting images from the simulation experiments. For both simulations with motion from Figure 5a and Figure 5b, compared to the reference image, the image without any compensation was clearly contaminated by motion artifacts (red arrow). After applying ME/MC to the measured data, most of the artifacts were suppressed (after 4 and 6 iterations of ME/MC, the improvement on motion estimation almost stopped). The corrected images were more similar to the truth image, as indicated by the higher SSIM.

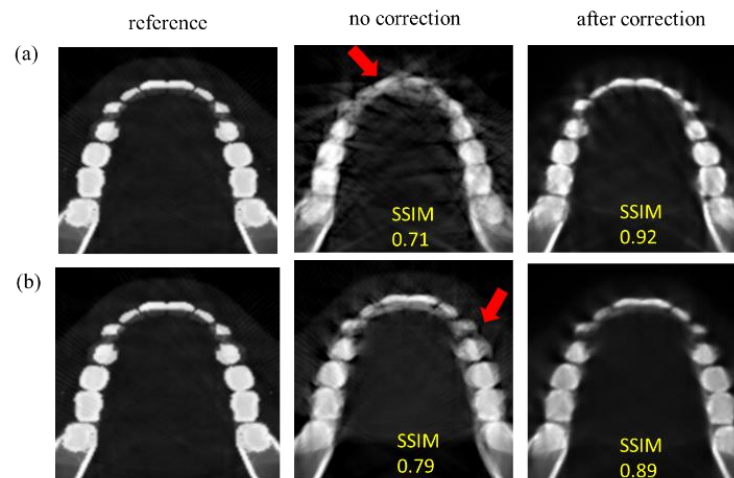


**Figure 6** Transaxial planes of (a) simulation with motion in Figure 5a and (b) simulation with motion in Figure 5b. After correction, most artifacts were successfully removed and details in the teeth were recovered. The SSIM of corrected and uncorrected images are listed alongside images. The display window is [-1000, 3000HU].

## 4. PHANTOM SCAN

### 4.A Phantom and motion

A phantom scan was performed on an 3D Accuitomo 170 scanner (Morita Inc., Kyoto, Japan) in Oral and Maxillo-facial Surgery Department of UZ Leuven. The anthropomorphic phantom model

is a Sectional Head Phantom SK150 (Phantom Laboratories, Salem, NY, USA). This phantom has an internal air cavity representing the oral, pharynx and trachea anatomy. The scan was a full rotation scan with 512 views. The total scan lasted for 17.5 s using continuous irradiation. Other scan parameters were: detector size 940×748, detector pixels of 0.2×0.2 mm<sup>2</sup>; scan FOV 140×100 mm<sup>2</sup>; distance between the X-ray source and the detector 842 mm; distance between the detector and the rotation center 302 mm.

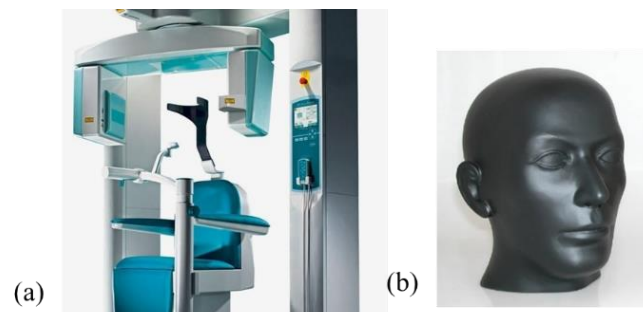


**Figure 7** (a) 3D Accuitomo 170 scanner <sup>26</sup> (b) The anthropomorphic phantom used in the experiment.

Motion was induced by pulling a string attached to the phantom in the middle of the scan, while having the phantom centered in the scanner FOV. After starting the acquisition (~5 s), the examiner pulled the string from outside the examining room. The induced motion was expected to create motion artifacts in the reconstructed image. Following the scan with induced movement, a static scan using the same scan parameters was performed as a reference.

#### **4.B Experiment design**

Similar to the simulation study, we aimed to compare the uncorrected, corrected and reference images. Details of how these images were obtained are listed below.

1. Reference image

Machine reconstructed image of the static scan was used as the reference image. The size of this image was 561×561×401, pixel size was 0.25×0.25×0.25 mm<sup>3</sup>.

## 2. Image w/o compensation

Machine reconstructed image of the scan with motion was also exported. The dimension of this image was the same as the reference image. No motion compensation or post-processing was applied.

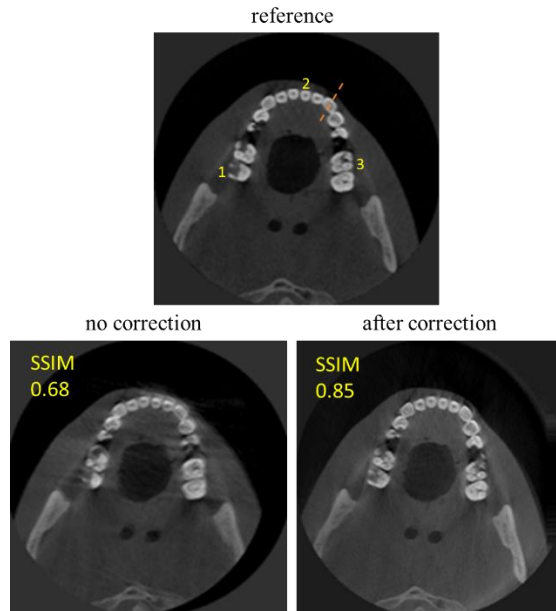
## 3. Image with ME/MC

For the moving scan, raw measurement data were exported. We want to estimate the movement during this scan based on the raw data. The high-res patch had a resolution of 0.25×0.25×0.25 mm<sup>3</sup>, while the low-res patch had 1×1×1 mm<sup>3</sup>. In one ME, re-projection was done by combining the forward projections of the two patches. ME/MC updated the image and the motion alternately, with a total number of 8 iterations of ME/MC performed. A final corrected image was obtained with an FDK algorithm with estimated motion as done in simulation studies. The pixel size was the same as the one of the reference image.

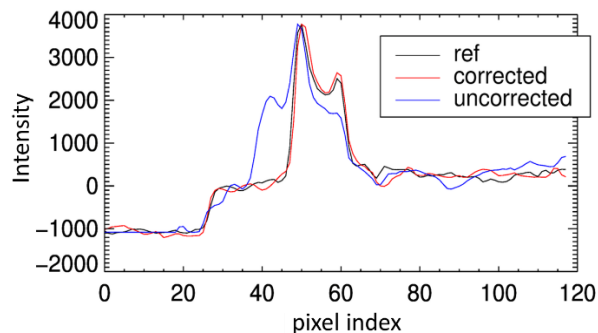
## 4.C Results

Figure 8 shows the selected planes of the above images. Compared to the reference image, the image without any compensation was clearly contaminated by motion artifacts and not suitable for diagnostic purposes or treatment plans. After applying proposed compensation method, most of the artifacts were suppressed. The SSIM of the corrected image to the reference image is higher than the one of uncorrected image. Figure 9 contains the profile plots across a tooth that describe the local differences. To quantify the local change of the sharpness, we also computed the gradient variance in three selected ROIs (containing one right molar, left molar and incisor

respectively) for all images. The gradient variance value of the teeth was increased after motion compensation (Table I).



**Figure 8** 2D transaxial planes of the reference, uncorrected and corrected images. Note that the “double edge” motion artifacts in the uncorrected image disappeared in the corrected one. Both dentists agreed that better visualization of bony structures was achieved after compensation. Three teeth to be measured for sharpness are labeled with number by their side. The display window is [-100, 3000HU].



**Figure 9** Profile plots over a canine tooth, in accordance with the orange line in Figure 8. The plot from the uncorrected image is considerably different from the other two.

## **5. PATIENT SCAN**

### **5.A Scan protocol**

A 9 year-old child with cleft lip and palate underwent CBCT scanning for the follow-up treatment. The reconstructed image was identified with visual motion artifacts and included in this study. This scan was acquired on the same scanner used in the phantom study and has a full rotation acquisition with 512 views, and a scan time of 17.5 s with continuous irradiation. Scan parameters were: detector size 940×748, detector pixels 0.2×0.2 mm<sup>2</sup>; scan FOV 100×50 mm<sup>2</sup>. Other parameters were the same as the ones used in the phantom study.

### **5.B Results**

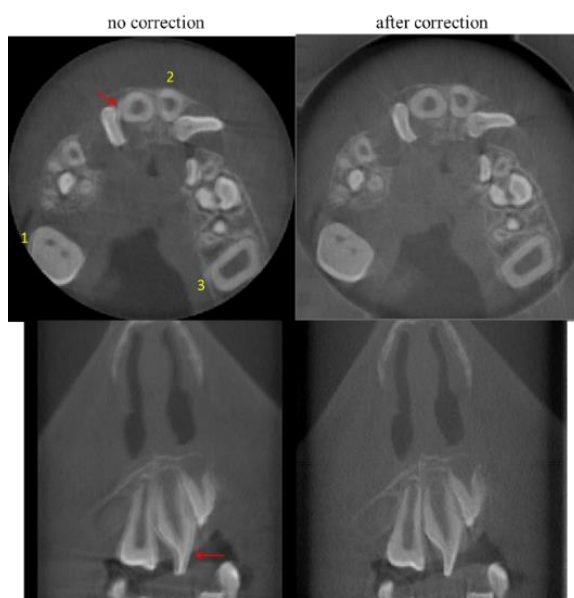
Because there was no reference (repeat) scan performed in the patient study, we only compared the motion-corrected image with the machine reconstructed image. The image size was 481×481×481, pixel size was 0.125×0.125×0.125 mm<sup>3</sup>. The high-res patch had a resolution of 0.125×0.125×0.125 mm<sup>3</sup>, while the low-res patch had 0.5×0.5×0.5 mm<sup>3</sup>. Motion was estimated by the proposed ME/MC scheme, and a final high-resolution FDK reconstruction was performed with the motion accounted for during backprojection to obtain the motion-corrected image.

Figure 10 and Figure 11 show selected transaxial and coronal planes of the corrected and uncorrected images. A total number of 4 iterations of ME/MC were performed. Two dentists assessed the reconstructed images. After applying the proposed method, most of the artifacts were suppressed, and certain diagnostic features were more visible. The image sharpness was also measured in a similar way as in the phantom study. In three selected ROIs (containing one

right molar, left molar, incisor), the gradient variance is considerably increased after compensation, which indicates the increase of image sharpness (Table I).

**Table I** Gradient variance (scaled by  $10^8$ ) as index of image sharpness in phantom and patient studies

	reference	no correction	after correction
right molar (phantom)	1.723	1.019	1.515
left molar (phantom)	0.830	0.103	0.562
incisor (phantom)	1.203	0.607	0.921
right molar (patient)	/	0.391	0.463
left molar (patient)	/	0.601	1.188
incisor (patient)	/	0.221	0.425



**Figure 10** Selected transaxial and coronal planes. After applying compensation, blurring and shading artifacts were reduced substantially. As for diagnostic difference, dentists could identify the contact between the front teeth (arrow) in the transaxial views after motion compensation but not before; also, structures of teeth (arrow) could be better differentiated in coronal views which is useful in diagnosis of dental pathology. Three teeth to be measured with sharpness are labeled with number by their side. The display window is [-1000, 4000HU].

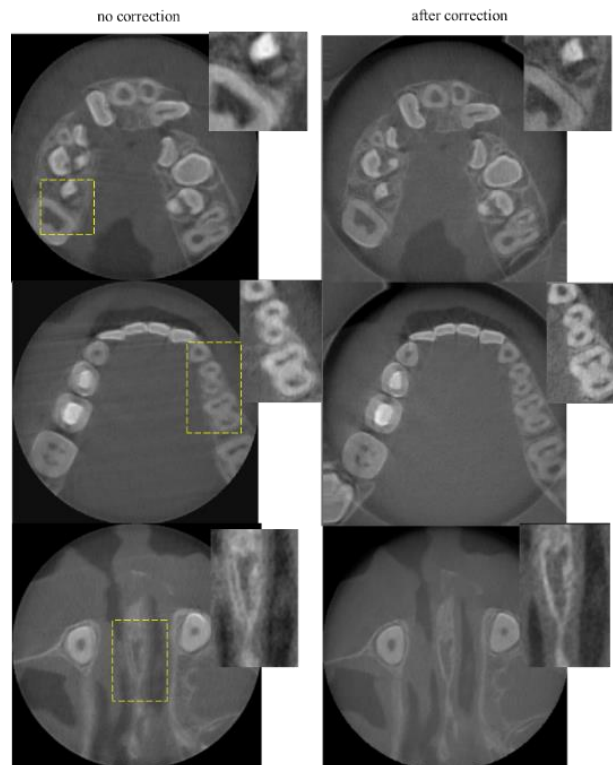


**Figure 11** In the selected position, the spatial resolution was improved substantially after correction. The display window is [-1000, 4000HU].

## 6. DISCUSSION

In this paper, we proposed a motion estimation and compensation approach for oral and maxillofacial CBCT imaging. It tolerated transaxial truncation and only required the measured raw

data. Since no additional measurements are needed, it can be applied retrospectively to a motion-contaminated dental scan data. The proposed method was evaluated in simulation, phantom and patient studies. After compensation, the quality of the reconstructed image was higher than that of the uncorrected one. The method would avoid the retake of the scan when patient moves, which can significantly reduce the radiation exposure, especially for children who are more likely to move than adults. This is even more important for a child with cleft lip and palate who often needs a series of scans at their early ages to guide the treatments.

Note that in all cases, the motion was assumed and modeled as rigid motion of an object across all projection views. In a more complicated scenario, a non-rigid movement of the tissues due to swallowing, or a different motion pattern between the upper and lower jaws, might be present in a scan. How to deal with such movements is beyond the scope of this paper. Also, together with motion, the presence of dental implants and other metallic objects like fillings and crowns could complicate the artifacts in a reconstruction image. A metal artifacts correction technique would have to be combined with the proposed motion compensation technique, to simultaneously mitigate the motion and metal artifacts <sup>27,28</sup>.

The proposed approach worked reasonably well despite severe artifacts outside the high-res patch, where the reconstruction is handicapped by a limited angle problem. It has been previously shown that the high-res patch can in principle be reconstructed exactly if it contains a portion of air background (intensity known to be zero) <sup>29</sup>, which is often the case in dental imaging. Moreover, even in the background, spatial frequencies are better reconstructed if they contribute more information to the measured projections (typically edges which are parallel to the projection lines). This implies that the reconstructed low-res patch still contains the relevant edges needed to align measured and forward projected views, which is the essence of the original ME/MC scheme.

Unlike a clinical helical CT scan, a normal oral and maxillofacial scan has a small number of views (300~700) acquired in a full or half rotation. Hence the computation requirement to apply

motion compensation in dental imaging is less demanding. The entire ME/MC process took ~2 hours (1.5 hour ME/MC iterations and 0.5 hour final reconstruction) for the given patient scan on a single core CPU. By introducing proper acceleration techniques (e.g. parallelization), the processing time can be significantly reduced.

There were still some remaining streak artifacts and blurring in the corrected images. These are possibly due to several limitations of the proposed method: 1) scattering and beam hardening effects were not corrected; 2) during the ME/MC iterations, the entire object is never reconstructed exactly due to the truncation, which may reduce the accuracy of motion estimation; 3) we assumed the movement only happens in between views. Because the motion during the acquisition of a single view is not compensated for, fast motions may produce a residual loss of resolution in the corrected images. Given the fact that the lag time in between views was negligible and the exposure time of one projection view in CBCT is ~30 ms, such movement within views might not be negligible. 4) the final FDK reconstruction is not exact when motion compensation is incorporated. However, we consider the overall motion in a dental scan is small, so one can use the analytical algorithm (e.g. FDK), with a first-order motion compensation during the back-projection step, without introducing significant artifacts. When motion is large, a dedicated FDK<sup>30,31</sup> or an iterative reconstruction algorithm may be appropriate for the final motion-compensated reconstruction.

Variation in scan protocol could affect the motion compensation. For example, a smaller size of the FOV captures less information in the measurement and increases the extent of truncation, which may degrade the motion estimation results. Offset scan mode is sometimes available on some scanners. With this scan mode, a small detector is used to scan a relatively large FOV, at the cost of increased and asymmetrical truncation in each view. But the asymmetrically truncated projections may present a challenge to motion estimation. It is expected a half scan typically suffers more from cone-beam artifacts, but less from motion artifacts due to the shorter scan time,

compared with a full rotation scan. For the same reason only using half of the measured views may result in a less artifacts-contaminated image, even for a full scan.

## **7. CONCLUSION**

In this study, we proposed an approach to suppress the motion artifacts in oral and maxillofacial imaging. Results from simulations, phantom and patient studies were presented. The improvement on the image quality was assessed both quantitatively and qualitatively. Further clinical evaluation with different scan protocol setups is needed.

## **ACKNOWLEDGEMENTS**

The authors want to thank Dr. Koen Michielsen and Dr. Guozhi Zhang for providing the digital phantom and helpful discussion.

## **CONFLICT OF INTEREST**

The authors report no conflicts of interest in conducting this research.

## **REFERENCES**

1. Yildizer Keriş E. Effect of patient anxiety on image motion artefacts in CBCT. *BMC Oral Health*. 2017;17(1):1-9.
2. Donaldson K, O'Connor S, Heath N. Dental cone beam CT image quality possibly reduced by patient movement. *Dentomaxillofacial Radiol*. 2013;42(2):3-4.

3. Spin-Neto R, Wenzel A. Patient movement and motion artefacts in cone beam computed tomography of the dentomaxillofacial region: A systematic literature review. *Oral Surg Oral Med Oral Pathol Oral Radiol.* 2016;121(4):425-433.
4. Pauwels R, Araki K, Siewerdsen JH, Thongvigitmanee SS. Technical aspects of dental CBCT: State of the art. *Dentomaxillofacial Radiol.* 2015;44(1):1-20.
5. Nardi C, Borri C, Regini F, et al. Metal and motion artifacts by cone beam computed tomography (CBCT) in dental and maxillofacial study. *Radiol Medica.* 2015;120(7):618-626.
6. Hanzelka T, Dusek J, Ocasek F, et al. Movement of the patient and the cone beam computed tomography scanner: Objectives and possible solutions. *Oral Surg Oral Med Oral Pathol Oral Radiol.* 2013;116(6):769-773.
7. Spin-Neto R, Matzen LH, Schropp L, Gottfredsen E, Wenzel A. Detection of patient movement during CBCT examination using video observation compared with an accelerometer-gyroscope tracking system. *Dentomaxillofacial Radiol.* 2017;46(2):1-7.
8. Eldib ME, Hegazy MAA, Cho MH, Cho MH, Lee SY. A motion artifact reduction method for dental CT based on subpixel-resolution image registration of projection data. *Comput Biol Med.* 2018;103(June 2019):232-243.
9. Bruder H, Rohkohl C, Stierstorfer K, Flohr T. Compensation of skull motion and breathing motion in CT using data-based and image-based metrics, respectively. In: *SPIE Medical Imaging.* Vol 9783. ; 2016:97831E.
10. Hernandez D, Eldib ME, Hegazy MAA, Cho MH, Cho MH, Lee SY. A head motion estimation algorithm for motion artifact correction in dental CT imaging. *Phys Med Biol.* 2018;63(6).

11. Kingston A, Sakellariou A, Varslot T, Myers G, Sheppard A. Reliable automatic alignment of tomographic projection data by passive auto-focus. *Med Phys*. 2011;38(9):4934-4945.
12. Kyriakou Y, Lapp RM, Hillebrand L, Ertel D, Kalender W a. Simultaneous misalignment correction for approximate circular cone-beam computed tomography. *Phys Med Biol*. 2008;53(22):6267-6289.
13. Sisniega A, Stayman J, Yorkston J, Siewerdsen J, Zbijewski W. Motion compensation in extremity cone-beam CT using a penalized image sharpness criterion. *Phys Med Biol*. 2017;62(9):3712-3734.
14. Sun T, Kim J, Fulton R, Nuyts J. An iterative projection-based motion estimation and compensation scheme for head X-ray CT. *Med Phys*. 2016;43(10):5705-5716.
15. Sun T, Nuyts J, Fulton R. A Motion Compensation Approach for Dental Cone-beam Region-of-interest Imaging. In: *International Meeting on Fully Three-Dimensional Image Reconstruction in Radiology and Nuclear Medicine*. ; 2017:299-302.
16. Hudson HM, Larkin RS. Ordered subsets of projection data. *IEEE Trans Med Imaging*. 1994;13(4):601-609.
17. Feldkamp LA, Davis LC, Kress JW. Practical cone-beam algorithm. *J Opt Soc Am A*. 1984;1(6):612-619.
18. Van Slambrouck K, Nuyts J. Reconstruction scheme for accelerated maximum likelihood reconstruction: The patchwork structure. *IEEE Trans Nucl Sci*. 2014;61(1):173-181. doi:10.1109/TNS.2013.2287637
19. Fessler JA, Ficaro EP, Clinthorne NH, Lange K. Grouped-coordinate ascent algorithms for penalized-likelihood transmission image reconstruction. *IEEE Trans Med Imaging*. 1997;16(2):166-175.

20. Yu L, Zou Y, Sidky EY, Pelizzari CA, Munro P, Pan X. Region of interest reconstruction from truncated data in circular cone-beam CT. *IEEE Trans Med Imaging*. 2006;25(7):869-881.
21. Van Slambrouck K, Nuyts J. Metal artifact reduction in computed tomography using local models in an image block-iterative scheme. *Med Phys*. 2012;39(11):7080-7093.  
doi:10.1118/1.4762567
22. Wang Z, Bovik AC, Sheikh HR, Simoncelli EP. Image quality assessment: From error visibility to structural similarity. *IEEE Trans Image Process*. 2004;13(4):600-612.
23. Bueno-Ibarra MA, Alvarez-Borrego J, Acho L, Chavez-Sanchez MC. Fast autofocus algorithm for automated microscopes. *Opt Eng*. 2005;44(6):63601.
24. De Man B, Basu S. Distance-driven projection and backprojection in three dimensions. *Phys Med Biol*. 2004;49(11):2463-2475.
25. Kim J, Sun T, Alcheikh AR, Kuncic Z, Nuyts J, Fulton R. Correction for human head motion in helical x-ray CT. *Phys Med Biol*. 2016;61(4):1416-1438.
26. 3D Accuitomo 170. <https://www.morita.com/group/en/products/ophthalmology/diagnostic-and-imaging-equipment/3d-accuitomo-170-1/?tab=configuration>
27. Sun T, Nuyts J, Fulton R. Simultaneous correction of motion and metal artifacts in head CT scanning. In: *IEEE Nuclear Science Symposium and Medical Imaging Conference*. ; 2017:1-3.
28. Hahn A, Knaup M, Brehm M, Sauppe S, Kachelrieß M. Two methods for reducing moving metal artifacts in cone-beam CT. *Med Phys*. 2018;45(8):3671-3680.  
doi:10.1002/mp.13060
29. Defrise M, Noo F, Clackdoyle R, Kudo H. Truncated Hilbert transform and image

reconstruction from limited tomographic data. *Inverse Probl.* 2006;22(3):1037-1053.

30. Jang S, Kim S, Kim M, Ra JB. Head motion correction based on filtered backprojection for x-ray CT imaging. *Med Phys.* 2018;45(2):589-604.
31. Sun T, Fulton R, Nuyts J. A method to reduce the data-redundancy artifacts for arbitrary source trajectories in CT imaging. In: *IEEE Nuclear Science Symposium and Medical Imaging Conference.* ; 2018:1-3.

**Figure 1** For every view, the centers of (a) the detector and (b) scanner coordinate systems coincide with each other.  $T_x$ ,  $T_y$ ,  $T_z$  are translations along coordinate axes.  $R_t$ ,  $R_s$ ,  $R_c$  are rotations around coordinate axes.

**Figure 2** Motion Estimation/ Motion Compensation (ME/MC) scheme in<sup>14</sup>. One iteration of ME/MC involves 1 ME step and 1 MC step. One ME step attempts to adjust the object pose at each view to minimize the difference between the measured projections and the re-projected object, with the help of auxiliary projections. One MC step compensates for the motion during the scan in the iterative reconstruction process, by incorporating the motion estimates into the system matrix.

**Figure 3** Schematic representation of an iteration of the MC reconstruction. A first update was only performed in the high-res patch, and a sequential update was performed in the low-res patch. The dashed circle indicates the fully sampled FOV, i.e. high-res patch.

**Figure 4** The digital phantom that used in the simulations. For left to right: selected transaxial, coronal and sagittal view.

**Figure 5** The recorded motion segments used to generate the motion-contaminated projections. Motion (a) is more abrupt while (b) is more continuous.  $R_t$ ,  $R_s$ ,  $R_c$ ,  $T_z$ ,  $T_x$ ,  $T_y$  were defined in Figure 1. Details of how it was recorded can be found in <sup>25</sup>.

**Figure 6** Transaxial planes of (a) simulation with motion in Figure 5a and (b) simulation with motion in Figure 5b. After correction, most artifacts were successfully removed and details in the teeth were recovered. The SSIM of corrected and uncorrected images are listed alongside images. The display window is [-1000, 3000HU].

**Figure 7** (a) 3D Accuitomo 170 scanner <sup>26</sup> (b) The anthropomorphic phantom used in the experiment.

**Figure 8** 2D transaxial planes of the reference, uncorrected and corrected images. Note that the “double edge” motion artifacts in the uncorrected image disappeared in the corrected one. Both dentists agreed that better visualization of bony structures was achieved after compensation. Three teeth to be measured for sharpness are labeled with number by their side. The display window is [-100, 3000HU].

**Figure 9** Profile plots over a canine tooth, in accordance with the orange line in Figure 8. The plot from the uncorrected image is considerably different from the other two.

**Figure 10** Selected transaxial and coronal planes. After applying compensation, blurring and shading artifacts were reduced substantially. As for diagnostic difference, dentists could identify the contact between the front teeth (arrow) in the transaxial views after motion compensation but not before; also, structures of teeth (arrow) could be better differentiated in coronal views which is useful in diagnosis of dental pathology. Three teeth to be measured with sharpness are labeled with number by their side. The display window is [-1000, 4000HU].

**Figure 11** In the selected position, the spatial resolution was improved substantially after correction. The display window is [-1000, 4000HU].